Development of a myocardial perfusion phantom

G.J. (Gijs) de Vries, s1854526

Revision 1.0

Development of a myocardial perfusion phantom

G.J. de Vries, s1854526

Tuesday 8th January, 2019

Preface

The project plan outlines an introduction and literature of the topic along with organisational information including a detailed planning.

G.J. (Gijs) de Vries
Enschede, 3$^{\text{rd}}$ December 2018

Contents

1 Introduction

Myocardial Perfusion Imaging (MPI), or, simply put, the imaging of the blood flow in the heart muscle, plays an important role in diagnosing heart failure or detecting Coronary Artery Disease (CAD). Imaging systems like Computed Tomography (CT), Magnetic Resonance Imaging (MRI), Single-Photon Emission Computed Tomography (SPECT), or Positron Emission Tomography (PET) can visualise a (radioactive) contrast bolus in the supplying arteries and in underlying myocardial tissue, whose flow can give an indication of narrowed or blocked blood vessels.

Many variations in the visualisation process of myocardial perfusion, including variations in hard- and software, can (significantly) influence the outcome and in turn have consequences for patient treatment. These variations need to be validated against a well-known baseline.

Document overview

The project plan consists of a literature review of existing myocardial perfusion phantoms, their comparison to human physiology, and a discussion between the different types of scanners. The literature is followed by the research methodology containing the research questions and goals of the project. The detailed planning is the last section of the project plan stating workdays and -weeks, off-days, deadlines, and meetings.

Abbreviations

AIF Arterial Input Function

CAD Coronary Artery Disease

CT Computed Tomography

CZT Cadmium Zinc Telluride

ECTS European Credit Transfer and Accumulation System

FWHM Full Width at Half Maximum

HU Hounsfield Unit

MPI Myocardial Perfusion Imaging

MRI Magnetic Resonance Imaging

MV Maximal Vasodilation

PA Pulmonary Artery

PET Positron Emission Tomography

PET-MR PET-Magnetic Resonance

PMT Photomultiplier Tube

PV Pulmonary Vein

SPECT Single-Photon Emission Computed Tomography

VC Vena Cava

2 Literature

2.1 Phantoms

2.1.1 Magnetic Resonance

Noguchi et al. (2007) developed a simple phantom that consists of a syringe, diameter of 40mm, beads, and tubes, diameter of 4mm. The perfusate, 0.1mM GD-DTPA doped 8L water solution, flows through the beads, to disturb the flow, and then perfuses through parallel tubes, to prevent cross-current. The perfusate is tagged at the beads while the images are taken at 5 parallel planes, perpendicular to the tubes. The actual measured flow is the average obtained from the parallel planes.

Ebrahimi et al. (2010) created a phantom using microfabrication to create a microvasculature on 4-inch ($\approx$ 10cm) silicone wafers. The microvasculature is build up from four blocks, containing 4x2 (RxC) cells. Each cell is build up from 100 "features" separated by $25\mu m$ tracks. These tracks provide many different paths for perfusate to flow, effectively simulating capillaries in tissue. A $300\mu L$ bolus of a distilled water solution containing 25mM/L of Manganese.

Wang et al. (2010) used a heamodialysis filter connected to a nonpulsatile pump. A static water phantom was placed next to the haemodialysis filter to show that it cancels out between tag (with magnetic labelling) and control (no magnetic labelling) images.

Anderson et al. (2011) extracted hollow fibres from haemodialysis filters to create their own single-fibre and multi-fibre phantom. Similar to some standard haemodialysis filters, their phantoms have access to both the extracellular space (i.e. the fluid outside of the fibres) and intracellular space (i.e. the fluid inside the fibres). As the name suggests, their single-fibre phantom consists of an individual fibre placed inside a capillary tube. The multi-fibre phantom consists of a variable amount of fibres that are placed in a heat-shrink tube. A four-way valve switched between the main perfusate and a aquesous solution of 0.2 mM GD-BOPTA.

Chiribiri et al. (2013b) developed a four chambered anatomic phantom that resembles the heart of a 60kg person. The four chambers correspond to the four chambers of the heart, sized to match the physiological size. In addition, a Vena Cava (VC), Pulmonary Artery (PA)/Pulmonary Vein (PV) combination, and an aorta are present in the phantom. Contrast is injected in the same manner as is performed in patients; in a vein. In the phantom, the contrast is injected directly into the vena cava via a three-way stopcock. The contrast moves through the phantom's right atrium, right ventricle then via the PA/PV to the left chamber and finally to the left ventricle. The phantom is not capable of simulating the contrast's behaviour in the lungs since the PA is directly connected to the PV. Two myocardial chambers (one active and one control), the VC, PA, PV and the aorta are in the imaging plane where the proximal part of the aorta, where the aorta branches to the myocardium, is used for the Arterial Input Function (AIF).

Otton et al. (2013) used the same phantom to compare CT against MRI. In addition to the previous authors, O'Doherty et al. (2017a) used a water-filled torso phantom to ensure more anatomically correct image in PET-Magnetic Resonance (PET-MR).

2.1.2 Computed Tomography

Teslow and Robb (1991) developed a cylindrical perfusion phantom, shaped like the left ventricle of a dog. It has a 6.5cm outer diameter, 4.5cm inner diameter, and a length of 6.5cm. The authors specifically used methyl methacrylate plastic since it gives similar radiographic image as tissue and blood. Additionally, a solid plastic cylinder, placed in the centre, is used to attenuate x-ray beams similar to the attenuation of a blood-filled dog's ventricle. The capillaries

are simulates by means of different sized nylon balls of 0.318, 0.476, and 0.635cm. The smallest balls are packed near the outlet, while the medium sized balls are packed at the inlet, and the largest balls are placed in between. The authors do not go into detail on the used contrast agent, other than 10ml of a radio-opaque indicator is injected for one second.

Klotz and König (1999) used a simple lucite cylinder, which had a 24mm inner diamter, and filled it with a 20mm column of small grannulae. The polystyrol had been heated and compressed to increase the density creating a perfusable volume of 20%. The lucite cylinder is placed in a 20cm water phantom and 1ml of contrast, Iopromide 370 mg/ml, is manually injected.

Driscoll et al. (2011) developed a 10cm long, with a diameter of 5cm, phantom with two inputs, only one is used, and two outputs. The capillaries are simulated by means of a vinyl tube where mass can be exchanged with the main cylinder via sets of small holes on either side of the cylinder. The output of the vinyl tube and the output of the shell combine, and feeds back through the imaging area to validate outward going flow, which should be the same as the input flow. Their AIF, however, is created by means of a programmable pump which injects in the form of a typical clinical AIF rather than having a system-based AIF. The Visipaque^{TM} (iodixanol) 270 mgI/ml is injected into a blood-mimicking fluid consisting of 40% glycerol and 60% water.

Ganguly et al. (2012) developed an interestingly, slightly different phantom than other; a linearly moving phantom. The phantom itself is a cylinder, 1.9cm inner diameter, with a length of 32.2cm. It contained 64 different compartments of 0.5cm in height separated by a 0.5mm thick carbon fibre wall. Every compartment had a single opening where contrast, 300mgI/Omnipaque, is injected. The concentration of contrast that is injected in subsequent compartments, resemble a sinusoidal signal. This phantom is placed on a linear motor which moves the phantom parallel to the patient's bed. The author's goal is to compare and determine the temporal accuracy of the imaging system. To simulate the attenuation of the head, a 15cm cylindrical, water-filled, phantom was placed around the perfusion phantom.

Mathys et al. (2012) developed a similar phantom that consists of two cylinders, a smaller (4cm diameter) inside a larger (11cm diameter) cylinder. Water flows via four tubes into the inner cylinder where it flows outward into the larger cylinder that contains 1.5mm polyoxymethylene globes as tissue replacement. The larger cylinder is drained by four holes. 2mL of contrast, Accupaque 300, is injected followed by 15 of saline at 5mL/s using a double-head injector.

Boese et al. (2013) developed a cylindrical phantom for brain perfusion measurements in a C-arm. Their phantom utilises a combination of large arteries, smaller arteries, and a sinter board for the capillaries. The main artery splits into smaller arteries which in turn splits into sixteen even smaller ones that connect to the sinter board. The upper two arteries have an inner diameter of 1.7mm representing the carotid arteries and the lower two arteries have an inner diameter of 1.0mm representing vertebral arteries. The authors used a very specific contrast injection protocol: relatively large pre-injection of 21mL NaCl, followed by a variable amount of Imeron 400, and ended by a 6mL post-injection of NaCl, all at 6mL/s.

Suzuki et al. (2017) designed a straight-forward CT phantom that uses a dry-type haemodialyser with a pressurised dialysate space to prevent the perfusate from leaving the hollow fibres. The authors varied the dose in order determine the effects on the perfusion indices. They maintained a constant volumetric flow, Q, and concluded that the perfusion indices are susceptible to dose conditions.

Hashimoto et al. (2018) used the same phantom in combination with a commercially synthetic bone layer such that quantification software recognises the phantom as a human head. Instead of varying the dose, the contrast injection protocol and the scanning interval are varied based on their hypothesis that it would increase the quantitative accuracy. However, they concluded that they are independent factors when using the b-SVD algorithm.

2.1.3   Ultrasound

Veltmann et al. (2002) designed a flow phantom that consists of a high- and low flow circuit. The high flow circuit consists of a *heated* reservoir flowing into a haemodialysis cartridge, which filters any residue micro-bubbles (contrast agent) and removes air bubbles, before entering a second haemodialysis cartridge, the perfusion cartridge. Perfusate that does not enter the capillaries is returned to the reservoir passing a variable resistance. The perfusate that does enter the capillaries of the perfusion cartridge, is controlled by a gear pump, which simultaneously acts as a variable flow resistance for the low flow circuit. After the gear pump, a third haemodialysis filter filters the microbubbles from the perfusate. The authors performed two different experiments, one with an unmodified haemodialysis filter and one with a haemodialysis filter that has the majority of the lower capillaries glued shut. The contrast agent tends to float, especially in the low flow circuit. By decreasing the number of perfused capillaries, the flow is made more homogeneous and avoids attenuation in the lower areas. Both Sakano et al. (2015) and Lohmaier et al. (2004) use this phantom setup.

Kim et al. (2016) performs perfusion experiments using ultrasound without adding any contrast. Similar to the CT and MR phantoms, a dialysis tube is used to mimic human capillaries. The dialysis tube is submerged in water and part of the plastic case was removed, replaced by a latex foil as proposed by Veltmann et al. (2002), such that it creates an acoustic window. More interestingly, Kim et al. (2016) use a secondary, 1Hz, peristaltic pump to simulate cardiac motion. Gauthier et al. (2011) uses a peristaltic pump after a renal dialysis cartridge to create a pulsatile, but constant, flow. They do not use a secondary pump for the extracellular space.

2.1.4   Positron Emission Tomography / Single-Photon Emission Computed Tomography

Although the phantoms are not specifically designed for PET or SPECT scanning, the previously mentioned phantoms can be an inspirational source for PET/SPECT phantoms. The different technology requires a new approach to some (or many) of the materials used.

2.1.5   Phantom discussion

The phantom by Chiribiri et al. (2013b) physically resembles a simplified heart (four chambers, aorta, vena cava). However, it is unable to simulate the diffusion of contrast into heart tissue or the interstitial space, as admitted by the authors and confirmed by Otton et al. (2013); O'Doherty et al. (2017a). Furthermore, Chiribiri et al. (2013b) mentioned that the blood flow resistance is, due to its complexity, lower than in patients and is unable to mimic cardiac defects. The contrast curves look realistic and the flow estimations are accurate. The findings of Otton et al. (2013) are similar; the contrast curves represent those obtained from clinical trials. The phantom can be used in a clinical MR scanner, which increases the reliability . Even with the addition of a water-filled torso phantom, it is still unable to mimic respiratory or cardiac motion (O'Doherty et al., 2017b).

The straight forward phantom of Suzuki et al. (2017) does not resemble the human brain, which caused problems in certain programs, and the capillary possessions is much greater than in clinical situations. This may ultimately compromise the reliability of the phantom to mimic clinical situations. Although Hashimoto et al. (2018) uses a commercially synthethic bone layer, the phantom does not simulate contrast uptake by surrounding tissue which does occur in myocardial perfusion measurements.

2.2   Physiology

Slart (2015) performed absolute quantification with ^{13}N-ammonia, using a 3-compartment Hutchins model, and determined some normal perfusion values: 60-95 mL/min/100g in rest, and 190-300 mL/min/100g in stress.

Uren et al. (1994) used PET to quantitatively determine the blood flow for patients in control groups and 35 that have a form of stenosis. During these measurements, heart rate, diastolic blood pressure, and mean arterial pressure were similar between both groups. However, the systolic blood pressure was significantly higher for patients with a form of stenosis compared to the control group. The measured myocardial blood flow is summarised in table 2.1 and shows the importance of quantitative perfusion measurements. Patients with more than 40% stenosis have 39 - 64% less absolute blood flow. When converted to mL/min/100g, the perfusion estimates are slightly higher than the estimates made by Slart (2015). It is worth to note that the estimates by Slart (2015) are 21 years later than the estimates of Uren et al. (1994).

	Control	Stenosis			
		<40%	40-59%	60-79%	>80%
Base line	1.13 ± 0.26	0.96 ± 0.19	1.25 ± 0.34	1.23 ± 0.57	0.92 ± 0.33
MV*	3.37 ± 1.25	3.44 ± 1.47	2.07 ± 0.83	1.51 ± 0.37	1.22 ± 0.36

Maximal Vasodilation (MV)

Table 2.1: Myocardial blood flow according to Uren et al. (1994). Perfusion values in mL/min/g.

Chiribiri et al. (2013a) used high-resolution pixel-wise perfusion maps using MRI to determine normal reference values of myocardial blood flow during rest and stress. Hyperaemia is induced by means of adenosine. They found normal values of 0.9 ± 0.3 and 2.3 ± 1.4 mL/min/g for rest and stress, respectively. Converted to mL/min/100g, it more closely corresponds to the estimates made by Slart (2015).

Ho et al. (2014) scanned 35 low-risk patients and 35 patients with documented CAD using dynamic CT perfusion imaging on a dual-source CT scanner. Their results are summarised in table 2.2. The rest myocardial blood flow is in the same range as found by Chiribiri et al. (2013a) and Slart (2015). However, during stress, the perfusion is significantly lower than the estimate of Chiribiri et al. (2013a) and Slart (2015). A potential reason is the stress-inducing method used by the authors; Ho et al. (2014) uses dipyridamole-stress CT protocol, Chiribiri et al. (2013a) uses adenosine, and Slart (2015) is unknown. Furthermore, the differences can be a result of the used technique; Ho et al. (2014) used CT, Chiribiri et al. (2013a) used MRI and Slart (2015) used PET.

	Low risk	Historic ischaemia	Previous infarction
Global rest	74.08 ± 16.3	82.29 ± 16.87	81.98 ± 18.54
Global stress	141.92 ± 30.83	107.95 ± 25.25	106.93 ± 32.91

Maximal Vasodilation (MV)

Table 2.2: Myocardial blood flow according to Ho et al. (2014). Perfusion values in mL/min/g.

These results show that, although there are similarities, there is still a difference in the quantitative myocardial perfusion results. With these results, it is not known what the true myocardial perfusion is, further showing the need for a proper baseline.

2.3 Technology

2.3.1 CT

CT utilises a rotating X-Ray source, positioned in a gantry. The X-Ray source projects a narrow beam through the patient, which in turn is captured by a sensor at the other side. Different tissues have different linear attenuation coefficients, i.e. Hounsfield Unit (HU) values. The HU scale is a linear transformation based on the linear attenuation coefficients of both water and air. Images taken while the X-Ray source is quickly rotated around the patient, are processed to create cross-sectional images by using, for example, smearing. After a full rotation, also

known as a slice, the patient is moved further into the CT scanner and a new slice is made. The slice thickness depends on the specific scanner used, but according to the National Institute of Biomedical Imaging and Bioengineering (2016), a slice is typically between 1 and 10mm. Suzuki et al. (2017) used 8mm, Mathys et al. (2012) used both 8 and 10mm, and Otton et al. (2013) even used 0.6mm. In addition to creating cross-sectional slices, consecutive slices can be stacked to create a 3D-image.

2.3.2 MRI

MRI scanners align protons in hydrogen nuclei using a magnetic field that is 60.000 times stronger than earth's magnetic field. This magnetic field aligns the axis of rotation of the protons parallel or anti-parallel to itself. A radio transmitter introduces energy by means of an electromagnetic wave to tip the magnetisation by 90 degrees which creates a transverse magnetisation. The axis of rotation remains untouched and is perpendicular to this transverse magnetisation. The magnetisation then generates an alternating voltage in the receiver coil of the MRI scanner which is called the MRI signal(Weishaupt et al., 2008). MRI scanners can differentiate between different tissues since the protons in the tissues return to their normal spins at different rates (Lewis, 2017).

2.3.3 PET

PET, currently the gold standard, scanners use radionuclides to produce an image of underlying tissue. These radionuclides are bonded to nutrients, e.g. glucose, to create radiotracers. PET scanners can, for example, determine the rate of consumption for glucose when the radiolabelled glucose accumulates in tissue (Berger, 2003) which can provide information on tumours (whether it is benign or malignant). The radionuclide decays, called beta decay, and releases a positron, also known as an anti-electron. The lifetime of such positron is very short in electron rich tissue. The kinetic energy is quickly lost, typically within 1 to 10mm, and will combine with an electron to form a positronium. The positronium state last approximately 10^-10 seconds before it annihilates. During this annihilation, two high-energy photons (Badawi, 1999), in the gamma-ray region of the electromagnetic spectrum with ten times more energy than X-Rays, are released. These photons travel in opposite directions. Using coincidence detection, the photon's path can be deduced which passes through the point of annihilation and is close to where the positron was initially emitted. The most common approach to determine the actual locations, within a few millimetres, is computed tomography. During a PET scan, all the counts by a specific detector pair are measured which is proportional to the integrated radioactivity along the line joining these two detectors; commonly refereed to as line integral data. The line integrals at different angles are converted to a 2D image which show the distribution of the molecule to which the radionuclide was attached to (Cherry and Dahlbom, 2006).

2.3.4 SPECT

The imaging camera in a typical SPECT scanner are scintillator-based gamma cameras, also known as Anger cameras. Gamma cameras use a scintillator to "transduce" gamma radiation, originating from an injected tracer, to photons. Part of these photons are directed towards a photocathode. If a quantum of light hits the photocathode, which has a photosensitive coating, electrons are emitted due to the photoelectric effect. These electrons travel through a Photomultiplier Tubes (PMTs) and hitting a series of dynodes, which in turn trigger secondary emission; effectively multiplying the number of electrons travelling through the tube. Electrons hitting the last dynode, which is known as the anode, cause a current pulse which can be detected by measuring equipment. It is proportional to the amount of gamma ray photons entering the scintillator(GE Healthcare, 2009).

Digital SPECT

Developments in imaging systems gave rise to the digital SPECT scanner. In contrast to the analogue Anger cameras, the digital SPECT scanner utilises a direct conversion semiconductor: Cadmium Zinc Telluride (CZT). Wagenaar (2004) used CZT to develop pixelated detector units which could then be used for medical imaging. In a recent study, it is shown that a digital SPECT scanner, using multiple pixelated CZT detectors, showed significant improvements in image sharpness and contrast (Goshen et al., 2018). These detector units do not require any PMTs and thus allow for a more compact and flexible design (Erlandsson et al., 2009). The D-SPECT scanner, a digital SPECT scanner developed by Spectrum Dynamics[1], offers improvements in sensitivity and energy resolution (Spectrum Dynamics, 2016) over Anger camera systems. However, these digital systems are relatively new and require proper validation to convince medical personnel of its value.

2.3.5 Scanner comparison

As is previously mentioned, there are various types of scanners that use different techniques, CT, MRI, or Scintigraphy based (SPECT/PET) scanners. Each having their own advantages and disadvantages.

Costs

Pelgrim et al. (2016) compares MRI against CT and the different theoretical models to acquire absolute perfusion measurements, and also mentioned the current gold standard in quantitative perfusion measurements: PET. PET scans are generally more expensive (Goel et al., 2014), as is shown by Hlatky et al. (2014) in their two year study. They showed that the costs for patients with suspected CAD using PET is 22% higher than SPECT, which is more widely used for coronary and myocardial perfusion measurements (Rahmim and Zaidi, 2008). However, with new tracers, specifically the ^{18}F-tracer flurpiridaz, the need for an on-site cyclotron will be eliminated (Pelgrim et al., 2016) potentially making PET scans more accessible.

Spatial resolution

State-of-the-art MRI and CT scanners offer better spatial and temporal resolution than PET/SPECT (Pelgrim et al., 2016; Khalil et al., 2011). MRI, in Myocardial Perfusion Imaging, can take three myocardial short-axis slices during 50-60 consecutive heartbeats with a spatial resolution of 1.5 x 1.5 x 10mm^3. Whole heart 3D perfusion MRI achieve a spatial resolution of 2.3 x 2.3 x 5mm^3 due to advanced accelerated imaging sequences. CT can achieve an even higher spatial resolution of 0.3 x 0.3 x 5mm^3.

Moses (2011) investigated current PET scanners and determines, theoretically, that the fundamental limit for the spatial resolution is 1.83mm for clinical PET cameras. Assuming that zero width detector elements are used. However, zero width detector elements are impractical, so Moses (2011) continues to state that a reasonable compromise would result in clinical PET cameras with a reconstructed spatial resolution of 2.36mm Full Width at Half Maximum (FWHM). Typical clinical PET scanners have a spatial resolution between 4 and 6mm while a clinical SPECT scanner has a spatial resolution between 8 and 12mm. Pre-clinical experiments suggest that there is still much to be achieved considering SPECT (Khalil et al., 2011). In these experiments, ≤1mm spatial resolution is achieved in SPECT scans, while PET achieves a spatial resolution between 1 and 2mm mainly due to non-reducible factors: positron range, distance from positron emission to annihilation, and non-collinear emission of gamma photons after annihilation. The digital SPECT scanners showed significant improvements over Anger based SPECT in image sharpness and contrast Goshen et al. (2018); Gambhir et al. (2009). No quant-

---

[1]https://www.spectrum-dynamics.com/

itative results have been given as to the increased performance of these solid-state detector systems.

Temporal resolution

The increased spatial resolution, of CT, comes at a price. The temporal resolution for dual-source CT scanners is 63ms but in order to achieve whole heart coverage, dynamic shuttling is used which reduces the time between scans to once every 2 - 3 heartbeats. More advanced scanners, with wider detectors, e.g. 256- and 320-slice CT, have lower temporal resolution (135ms) but image the whole heart without shuttling. Temporal resolution of MRI is typically in the order of 1 second. In spite of the increased spatial resolution, the advanced accelerated imaging sequence has a reduced temporal resolution making it unfit for quantitative estimation of myocardial blood flow(Pelgrim et al., 2016).

Radiation

A big limitation of CT, is the patient's exposure to ionising radiation. Every image that is taken, introduces additional radiation to the patient which could pose serious health risks. Both SPECT and PET rely on radioactive tracers for imaging purposes. MRI does not rely on ionising radiation and therefore does not have this limitation.

Contrast

Khalil et al. (2011) states that the soft tissue contrast in MRI is better than in CT. Additionally, MRI achieves better results without a contrast agent while CT depends on it. PET has poor tissue contrast since it can only visualise the radioactive tracer.

3 Research methodology

Different perfusion phantoms have been developed. Some are specifically designed to simulate the myocardial perfusion [1], others for brain perfusion [2], or capillaries in general [3], and even phantoms to simulate perfusion in rheumatoid finger joints (Sakano et al., 2015) and skin (Kim et al., 2018). Most software packages are designed for human organs and look for landmarks such that it can perform the most optimal calculation. Many of these phantoms do not resemble human anatomy. The phantom proposed by Chiribiri et al. (2013b), the four-chambered heart, comes close to mimicking a human heart. However, the myocardium chamber is simplified and not covering the chambers. Furthermore, the phantoms are unable to mimic cardiac defects. These anatomical anomalies, and the inability to mimic cardiac defects, results in the need for a new phantom.

3.1 Research questions

Can patient treatment reliably depend on the D-SPECT, using dynamic scanning, in myocardial perfusion imaging?

3.1.1 Primary goal

The goal of the project is to develop a prototype myocardial perfusion phantom capable of reproducible simulations of typical and cardiac defect situations using clinical software commonly used in myocardial perfusion scans. Most software packages require anatomical landmarks which imposes requirements on the phantom. In addition, the phantom can be used for educational and training purposes to demonstrate the impact of (poorly) chosen variables, e.g. pressure or flow, scanning parameters, cardiac defects, and so forth.

The primary goal is not to validate the D-SPECT, but to design and build a tool for that validation purpose. The project itself is carried out using the V-Model (Rook, 1986; Osborne et al., 2005) approach, see figure 3.1. Sub-research questions are based on this V-Model approach such that each phase has its own goal.
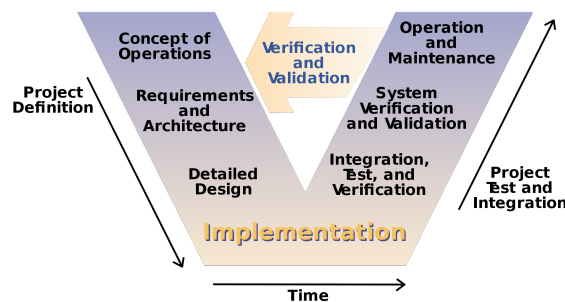
Figure 3.1: V-Model(Rook, 1986) as proposed by Osborne et al. (2005)

---

[1](Chiribiri et al., 2013b; Otton et al., 2013; O'Doherty et al., 2017a,b; Teslow and Robb, 1991)

[2](Hashimoto et al., 2018; Suzuki et al., 2017; Boese et al., 2013; Mathys et al., 2012; Ebrahimi et al., 2010; Wang et al., 2010; Noguchi et al., 2007; Ganguly et al., 2012; Klotz and König, 1999)

[3](Kim et al., 2016; Anderson et al., 2011; Driscoll et al., 2011; Gauthier et al., 2011; Veltmann et al., 2002; Lohmaier et al., 2004)

3.1.2 Concept of operations

Is the D-SPECT, in comparison with other types of scanners (CT, MRI, PET, or SPECT), for myocardial perfusion imaging accurate and reliable?

What must the myocardial perfusion phantom be able to simulate?

3.1.3 Requirements and Architecture

What are the requirements for a myocardial perfusion phantom that can be used in combination with commonly used clinical software?

3.1.4 Detailed Design

How can the myocardial perfusion phantom meet the clinical requirements and mimic the perfusion of a human heart?

3.1.5 Implementation and verification

Does the prototype myocardial perfusion phantom meet the specified requirements?

3.1.6 Secondary goal

During the individual project, a calibration set-up for flow and pressure sensors has been developed. The prototype version showed that flow sensors can be calibrated using the "emptying tank" principle. Pressure sensors have not been implemented in the prototype. Furthermore, the calibration set-up relies too much on human interaction. A sub-goal of the project will be to improve the existing calibration set-up such that flow and pressure sensors can be calibrated which in turn will increase the reliability of the flow set-up.

3.2 Stakeholders

A distinction is made between direct stakeholders, actively involved in the development, indirect stakeholders, can provide knowledge or resources, and beneficial stakeholders, (potentially) benefit from the development.

Direct	Indirect	Beneficial
- C.H. (Kees) Slump,	- M.J.W. (Marcel) Greuter,	- Patients with suspected CAD,
- M.E. (Marije) Kamphuis,	- R.H.J.A. (Riemer) Slart,	- Scanner manufacturers,
- Clinical Physicists,	- W.L. (Willem) van Meurs.	- Scanner software developers,
- Lab technicians,		- Hospitals,
- Nuclear Medicine Physicians,		- Physicians.
- Cardiologists.		

3.3 Approach

The research questions will primarily be answered by means of literature and by interviews with the stakeholders, see section 3.2. They are regularly involved with myocardial perfusion imaging and are thus familiar with the clinical software, hardware, work flow, and requirements. These interviews will provide additional (practical) insight.

Part of the V-Model approach is the continuous feedback. Requirements and designs are constantly updated according to new insights acquired during the development process.

3.3.1 General concept

A general concept is shown in figure 3.2. Three main parts can be identified: flow set-up, phantom, and imaging device. The flow set-up consists of everything to produce and maintain pressures and/or flows and measure these variables. The user-interface is a computer or

laptop. The phantom consist of everything needed to mimic cardiac defects and to provide a representative image for myocardial perfusion image processing software. The imaging set-up consists of the imaging device itself along with any contrast agents needed to properly image the phantom. Many imaging devices communicate with a dedicated workstation on which the image processing software runs.

3.4   Boundaries

The project is carried out as an Electrical Engineering's final thesis project of 40 European Credit Transfer and Accumulation System (ECTS). The boundaries for the project is to design and build a flow phantom capable of simulating myocardial blood flow according to specified, and agreed upon, system requirements. These system requirements require research, interviews and knowledge on physiology and are thus part of the project. The phantom and its set-up are part of research performed by M.E. (Marije) Kamphuis and imposes additional requirements on the project. The project is a tool for Marije to answer her research questions, but answering these research questions is not part of the final thesis.

3.5   Additional resources

During the individual project of G.J. (Gijs) de Vries, a prototype flow set-up, control module, and calibration set-up has been realised and can be used / re-cycled.

3.5.1   Flow set-up

The flow set-up uses simple, low costs pumps and available flow sensors. These might not be suitable for high precision flow systems. It is encouraged to look into alternatives.

3.5.2   Control module

The control module requires improvement when it is to be re-used. Two of the main improvements consist of improving the electro(magnetic) shielding to decrease the susceptibility to noise and to optimise the pump controllers.
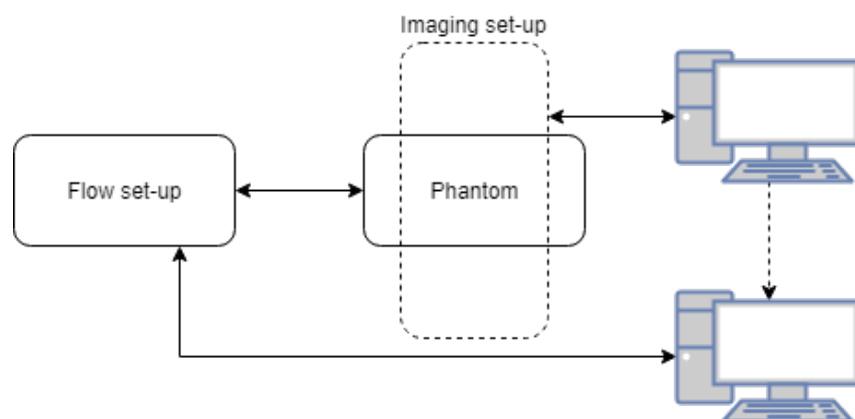

Figure 3.2: General concept, schematic

4 Planning

This chapter details the planning for the 40ECTS final thesis, carried out under the Robotics and Mechatronics Chair of the University of Twente. The project will be caried out in two phases; proof-of-concept (phase 1) and definitive (phase 2). The Gantt planning for phase 1 and 2 can be found in appendix B in figures B.1 and B.2 respectively.

4.1 Workdays

The planning is based on 28 hours per European Credit as per Dutch standard. The final thesis is carried out full-time (40 hours per week). The overview of working hours is shown in table 4.1.

Day	Start time	End time	Productive hours
Monday	08^{30}	16^{00}	7
Tuesday	08^{30}	17^{00}	8
Wednesday	08^{30}	16^{00}	7
Thursday	08^{30}	17^{00}	8
Friday	08^{30}	17^{00}	8
Miscellaneous*			2
Total:			40

* Miscellaneous hours are in evenings, weekends or during train rides.

Table 4.1: Workdays and -hours

4.2 Work weeks

The works weeks can be found in table A.1 in appendix A.

The project planning spans 35 weeks. Activities are planned from week 49 of 2018 up until, and including, week 28 of 2019 which spans a total of 32 weeks. Week 29 will be used to finalise practical aspects; handing in material and documentation, report printing, and so forth. The graduation presentation (and ceremony) will additionally take place in week 29. Weeks 30 and 31 of 2019 can serve as an extension if, and only if, approved by the assessment- and exam committee.

The planning takes into account one week around Christmas and new-years, one week spring break ("voorjaarsvakantie") in 2019, and a two week buffer. See section 4.3 for more details.

4.3   off-days

The University of Twente recognises three general holidays, New Year's day, King's Birthday and Liberation day, and six Christian holidays, Good Friday, Easter Monday, Ascension day, Whit Monday, Christmas day, and Boxing day[1]. Furthermore, the university recognises five bridging days in 2018 and fout bridging days in 2019 [2].

Both the King's Birthday as well as Liberation day fall in weekends. The remainder of the holidays and bridging days are summarised in table 4.2.

Holiday	Date	Note
Bridging day	2018 December 24	*Collective closure[2]*
Christmas day	2018 December 25	*Christian holiday[1]*
Boxing day	2018 December 26	*Christian holiday[1]*
Bridging day	2018 December 27	*Collective closure[2]*
Bridging day	2018 December 28	*Collective closure[2]*
Bridging day	2018 December 31	*Collective closure[2]*
New Year's day	2019 January 1	General holidays[1]
Good Friday	2019 April 19	*Christian holiday[1]*
Easter Monday	2019 April 22	*Christian holiday[1]*
Ascension Day	2019 May 30	*Christian holiday[1]*
Bridging day	2019 May 31	*Collective closure[2]*
Whit Monday	2019 June 10	*Christian holiday[1]*

Table 4.2: Off-days

Week 4 of 2019 is a planned vacation and no work will be done. This off-week spans from Monday 21st of January 2019 until, and including, Friday 25th of January 2019.

Currently, three lectures are planned which will result in an absent from the workplace in order to follow these lectures. These lectures are summarised in table 4.3.

What	Day	Date	When	Where
CT lecture	Thursday	2018 December 20	13^{45} - 17^{30}	Waaijer 2
PET lecture*	Thursday	2019 January 10	10^{45} - 12^{30}	HR C101
PET/SPECT Radiology	Monday	2019 January 14	08^{45} - 12^{30}	NH207

* Due to an in-house emergency service training ("BHV"), G.J. (Gijs) de Vries cannot attend this lecture.

Table 4.3: Planned lectures

---

[1] https://www.utwente.nl/en/ces/planning-schedules/academic-calendar/holidays-closing-days/

[2] https://www.utwente.nl/en/hr/terms-of-employment/scope-of-employment/public-holidays-leave-days/#compulsory-leave-days

4.4 Deadlines

The deadlines for phase 1 are shown in table 4.4 and those for phase 2 are shown in table 4.5.

What	R	Day	Date	Note
Project plan	0.1	Friday	2018 December 20	Before 2018 December 10
	0.2	Tuesday	2018 December 18	Before 2018 December 19
	1.0	Friday	2018 December 21	Before Christmas
System requirements	0.1	Friday	2019 January 11	
	0.2	Friday	2019 February 1	
	1.0	Friday	2019 February 8	
Design	concept	Friday	2019 March 1	
	choice	Monday	2019 March 4	
	final	Friday	2019 March 15	Parallel development
Realisation		Friday	2019 March 29	Including testing

Deadlines subject to change depending on weekly meetings

Table 4.4: Deadlines phase 1

What	R	Day	Date	Note
Project plan	1.1	Friday	2019 April 5	
	2.0	Friday	2019 April 12	
System requirements	1.1	Friday	2019 April 26	
	2.0	Friday	2019 May 3	
Design	concept	Friday	2019 May 24	
	choice	Monday	2019 May 27	
	final	Friday	2019 June 7	
Realisation		Friday	2019 July 12	Including testing
Final report	0.1	Friday	2019 June 14	
	0.2	Friday	2019 June 28	
	1.0	Friday	2019 July 12	

Deadlines subject to change depending on weekly meetings

Table 4.5: Deadlines phase 2

4.5 Meetings

Two types of progress meetings will be regularly planned. Weekly progress meetings between M.E. (Marije) Kamphuis and G.J. (Gijs) de Vries, and progress meetings every four to six weeks where C.H. (Kees) Slump joins. The weekly progress meetings will, unless otherwise discussed, take place on Tuesdays at 09^{00}.

What	Day	When	Participants
Progress meeting	Monday	2018 December 10, 14^{00}	G.J. (Gijs) de Vries, M.E. (Marije) Kamphuis, C.H. (Kees) Slump.
Progress meeting	Wednesday	2018 December 19, 15^{30}	G.J. (Gijs) de Vries, M.E. (Marije) Kamphuis, C.H. (Kees) Slump.
Work meeting	Tuesday	2019 January 8, 09^{30}	G.J. (Gijs) de Vries, M.E. (Marije) Kamphuis.
Orientation intro ZGT	Tuesday	2019 January 11/18	G.J. (Gijs) de Vries, M.E. (Marije) Kamphuis.
Progress meeting	Tuesday	2019 January 15, 13^{00}	G.J. (Gijs) de Vries, M.E. (Marije) Kamphuis, C.H. (Kees) Slump.
To be filled			

* will be planned on this day.

Will be updated when new meetings are planned. Does not relate to weekly recurring meetings

Table 4.6: Planned meetings

A Appendix: Work weeks

Week	Monday	Working	Note
49	2018 December 3	Yes	
50	2018 December 10	Yes	
51	2018 December 17	Yes	
52	2018 December 24	Partly	*See off-days*
1	2018 December 31	Mostly	*See off-days*
2	2019 January 7	Mostly	*CT college*
3	2019 January 14	Mostly	*PET college*
4	2019 January 21	No	*Vacation*
5	2019 January 28	Yes	
6	2019 February 4	Yes	
7	2019 February 11	Yes	
8	2019 February 18	Yes	
9	2019 February 25	Yes	
10	2019 March 4	Yes	
11	2019 March 11	Yes	
12	2019 March 18	Yes	
13	2019 March 25	Yes	
14	2019 April 1	Yes	
15	2019 April 8	Yes	
16	2019 April 15	Mostly	*See off-days*
17	2019 April 22	Mostly	*See off-days*
18	2019 April 29	Yes	
19	2019 May 6	Yes	
20	2019 May 13	Yes	
21	2019 May 20	Yes	
22	2019 May 27	Mostly	*See off-days*
23	2019 June 3	Yes	
24	2019 June 10	Mostly	*See off-days*
25	2019 June 17	Yes	
26	2019 June 24	Yes	
27	2019 July 1	Yes	
28	2019 July 8	Yes	
29	2019 July 15	Yes	
30	2019 July 22	No	*Extension when needed*
31	2019 July 29	No	*Extension when needed*

Table A.1: Work weeks

B Appendix: Gantt planning

Figure B.1: Phase 1 project planning

Figure B.2: Phase 2 project planning

Bibliography

Anderson, J., J. Ackerman and J. Garbow (2011), Semipermeable hollow fiber phantoms for development and validation of perfusion-sensitive mr methods and signal models, **vol. 39**, no.3, pp. 149–158.

Badawi, R. (1999), The physical principles of PET.
https://depts.washington.edu/nucmed/IRL/pet_intro/intro_src/section2.html

Berger, A. (2003), Positron Emission Tomography.
https://www.ncbi.nlm.nih.gov/pmc/articles/PMC1126321/

Boese, A., S. Gugel, S. Serowy, J. Purmann, G. Rose, O. Beuing, M. Skalej, Y. Kyriakou and Y. Deuerling-Zheng (2013), Performance evaluation of a C-Arm CT perfusion phantom, **vol. 8**, no.5, pp. 799–807.

Cherry, S. R. and M. Dahlbom (2006), PET: physics, instrumentation, and scanners, in *PET*, Springer, pp. 1–117.

Chiribiri, A., G. Morton, A. Schuster, E. Sammut, G. Hautvast, M. Breeuwer, N. Zarinabad and E. Nagel (2013a), Normal myocardial perfusion values on high-resolution pixel-wise perfusion maps, **vol. 15**, no.1, p. P21.

Chiribiri, A., A. Schuster, M. Ishida, G. Hautvast, N. Zarinabad, G. Morton, J. Otton, S. Plein, M. Breeuwer, P. Batchelor et al. (2013b), Perfusion phantom: An efficient and reproducible method to simulate myocardial first-pass perfusion measurements with cardiovascular magnetic resonance, **vol. 69**, no.3, pp. 698–707.

Driscoll, B., H. Keller and C. Coolens (2011), Development of a dynamic flow imaging phantom for dynamic contrast-enhanced CT, **vol. 38**, no.8, pp. 4866–4880.

Ebrahimi, B., S. D. Swanson and T. E. Chupp (2010), A microfabricated phantom for quantitative MR perfusion measurements: validation of singular value decomposition deconvolution method, **vol. 57**, no.11, pp. 2730–2736.

Erlandsson, K., K. Kacperski, D. Van Gramberg and B. F. Hutton (2009), Performance evaluation of D-SPECT: a novel SPECT system for nuclear cardiology, **vol. 54**, no.9, p. 2635.

Gambhir, S. S., D. S. Berman, J. Ziffer, M. Nagler, M. Sandler, J. Patton, B. Hutton, T. Sharir, S. B. Haim and S. B. Haim (2009), A novel high-sensitivity rapid-acquisition single-photon cardiac imaging camera, **vol. 50**, no.4, p. 635.

Ganguly, A., A. Fieselmann, J. Boese, C. Rohkohl, J. Hornegger and R. Fahrig (2012), In vitro evaluation of the imaging accuracy of C-arm conebeam CT in cerebral perfusion imaging, **vol. 39**, no.11, pp. 6652–6659.

Gauthier, T. P., M. A. Averkiou and E. L. Leen (2011), Perfusion quantification using dynamic contrast-enhanced ultrasound: The impact of dynamic range and gain on time–intensity curves, **vol. 51**, no.1, pp. 102–106.

GE Healthcare (2009), CZT Technology: Fundamentals and Applications, Technical report, General Electric Company.

Goel, A., D. Smith and C. Hakcing (2014), SPECT vs PET.
https://radiopaedia.org/articles/spect-vs-pet

Goshen, E., L. Beilin, E. Stern, T. Kenig, R. Goldkorn and S. Ben-Haim (2018), Feasibility study of a novel general purpose CZT-based digital SPECT camera: initial clinical results, **vol. 5**, no.1, p. 6.

Hashimoto, H., K. Suzuki, E. Okaniwa, H. Iimura, K. Abe and S. Sakai (2018), The effect of scan interval and bolus length on the quantitative accuracy of cerebral computed tomography

perfusion analysis using a hollow-fiber phantom, **vol. 11**, no.1, pp. 13–19.

Hlatky, M. A., D. Shilane, R. Hachamovitch, M. F. DiCarli, S. Investigators et al. (2014), Economic outcomes in the study of myocardial perfusion and coronary anatomy imaging roles in coronary artery disease registry: the SPARC study, **vol. 63**, no.10, pp. 1002–1008.

Ho, K.-T., H.-Y. Ong, G. Tan and Q.-W. Yong (2014), Dynamic CT myocardial perfusion measurements of resting and hyperaemic blood flow in low-risk subjects with 128-slice dual-source CT, **vol. 16**, no.3, pp. 300–306.

Khalil, M. M., J. L. Tremoleda, T. B. Bayomy and W. Gsell (2011), Molecular SPECT imaging: an overview, *International journal of molecular imaging*, **vol. 2011**.

Kim, M., C. K. Abbey and M. F. Insana (2016), Efficiency of US Tissue Perfusion Estimators, **vol. 63**, no.8, pp. 1131–1139.

Kim, M., Y. Zhu, J. Hedhli, L. W. Dobrucki and M. F. Insana (2018), Multidimensional Clutter Filter Optimization for Ultrasonic Perfusion Imaging, **vol. 65**, no.11, pp. 2020–2029.

Klotz, E. and M. König (1999), Perfusion measurements of the brain: using dynamic CT for the quantitative assessment of cerebral ischemia in acute stroke, **vol. 30**, no.3, pp. 170–184.

Lewis, T. (2017), What is an MRI (Magnetic Resonance Imaging)? https://www.livescience.com/39074-what-is-an-mri.html

Lohmaier, S., A. Ghanem, C. Veltmann, T. Sommer, M. Bruce and K. Tiemann (2004), In vitro and in vivo studies on continuous echo-contrast application strategies using SonoVue in a newly developed rotating pump setup, **vol. 30**, no.9, pp. 1145–1151.

Mathys, C., K. Rybacki, H.-j. Wittsack, R. S. Lanzman, F. R. Miese, S. Macht, S. Eicker, G. M. zu Hörste, G. Antoch and B. Turowski (2012), A phantom approach to interscanner comparability of computed tomographic brain perfusion parameters, **vol. 36**, no.6, pp. 732–738.

Moses, W. W. (2011), Fundamental limits of spatial resolution in PET, *Nuclear Instruments and Methods in Physics Research Section A: Accelerators, Spectrometers, Detectors and Associated Equipment*, **vol. 648**, pp. S236–S240.

National Institute of Biomedical Imaging and Bioengineering (2016), Computed Tomogrpahy (CT). https://www.nibib.nih.gov/science-education/science-topics/computed-tomography-ct

Noguchi, T., T. Yoshiura, A. Hiwatashi, O. Togao, K. Yamashita, K. Kobayashi, F. Mihara and H. Honda (2007), Quantitative perfusion imaging with pulsed arterial spin labeling: a phantom study, **vol. 6**, no.2, pp. 91–97.

O'Doherty, J., Z. Chalampalakis, P. Schleyer, M. S. Nazir, A. Chiribiri and P. K. Marsden (2017a), The effect of high count rates on cardiac perfusion quantification in a simultaneous PET-MR system using a cardiac perfusion phantom, **vol. 4**, no.1, p. 31.

O'Doherty, J., E. Sammut, P. Schleyer, J. Stirling, M. S. Nazir, P. K. Marsden and A. Chiribiri (2017b), Feasibility of simultaneous PET-MR perfusion using a novel cardiac perfusion phantom, **vol. 1**, no.1, p. 4.

Osborne, L. F., J. Brummond, R. Hart, M. Zarean, S. M. Conger et al. (2005), Clarus: Concept of operations, Technical report, United States. Federal Highway Administration.

Otton, J., G. Morton, A. Schuster, B. Bigalke, R. Marano, L. Olivotti, E. Nagel and A. Chiribiri (2013), A direct comparison of the sensitivity of CT and MR cardiac perfusion using a myocardial perfusion phantom, **vol. 7**, no.2, pp. 117–124.

Pelgrim, G., A. Handayani, H. Dijkstra, N. Prakken, R. Slart, M. Oudkerk, P. Van Ooijen, R. Vliegenthart and P. Sijens (2016), Quantitative myocardial perfusion with dynamic contrast-enhanced imaging in MRI and CT: theoretical models and current

implementation, *BioMed research international*, **vol. 2016**.

Rahmim, A. and H. Zaidi (2008), PET versus SPECT: strengths, limitations and challenges, **vol. 29**, no.3, pp. 193–207.

Rook, P. (1986), Controlling software projects, **vol. 1**, no.1, p. 7.

Sakano, R., T. Kamishima, M. Nishida and T. Horie (2015), Power Doppler signal calibration between ultrasound machines by use of a capillary-flow phantom for pannus vascularity in rheumatoid finger joints: a basic study, **vol. 8**, no.1, pp. 120–124.

Slart, R. (2015), Myocard perfusion: SPECT(CT) and PET(CT).

Spectrum Dynamics (2016), D-SPECT, Where It All Starts... Nine Digital CZT-Based Detectors. https://www.spectrum-dynamics.com/ d-spect-solid-state-technology9-digital-czt-based-detectors/

Suzuki, K., H. Hashimoto, E. Okaniwa, H. Iimura, S. Suzaki, K. Abe and S. Sakai (2017), Quantitative accuracy of computed tomography perfusion under low-dose conditions, measured using a hollow-fiber phantom, **vol. 35**, no.7, pp. 373–380.

Teslow, T. and R. Robb (1991), X-ray computed tomographic (CT) phantom designed for the development of techniques for measurement of myocardial perfusion, **vol. 36**, no.10, p. 1407.

Uren, N. G., J. A. Melin, B. De Bruyne, W. Wijns, T. Baudhuin and P. G. Camici (1994), Relation between myocardial blood flow and the severity of coronary-artery stenosis, **vol. 330**, no.25, pp. 1782–1788.

Veltmann, C., S. Lohmaier, T. Schlosser, S. Shai, A. Ehlgen, C. Pohl, H. Becher and K. Tiemann (2002), On the design of a capillary flow phantom for the evaluation of ultrasound contrast agents at very low flow velocities, **vol. 28**, no.5, pp. 625–634.

Wagenaar, D. J. (2004), CdTe and CdZnTe semiconductor detectors for nuclear medicine imaging, in *Emission Tomography*, Elsevier, pp. 269–291.

Wang, Y., S.-E. Kim, E. V. DiBella and D. L. Parker (2010), Flow measurement in MRI using arterial spin labeling with cumulative readout pulses—Theory and validation, **vol. 37**, no.11, pp. 5801–5810.

Weishaupt, D., V. D. Köchli and B. Marincek (2008), *How does MRI work?: an introduction to the physics and function of magnetic resonance imaging*, Springer Science & Business Media.